The evolutions of spin density and energy flux of strongly focused standard full Poincaré beams
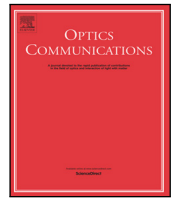
Man, Zhongsheng; Dou, Xiujie; Urbach, Hendrik Paul

Important note
To cite this publication, please use the final published version (if applicable).
Please check the document version above.

The evolutions of spin density and energy flux of strongly focused standard full Poincaré beams

Zhongsheng Man [a,b,c,*], Xiujie Dou [b], Hendrik Paul Urbach [b]

[a] School of Physics and Optoelectronic Engineering, Shandong University of Technology, Zibo 255000, China
[b] Optics Research Group, Delft University of Technology, Department of Imaging Physics, Lorentzweg 1, 2628CJ Delft, The Netherlands
[c] Collaborative Innovation Center of Light Manipulations and Applications, Shandong Normal University, Jinan 250358, China

ARTICLE INFO

ABSTRACT

Nonzero transverse spin density, which describes phenomenon in which the electromagnetic fields of localized light spin in a plane containing its wavenumber vector, has gained enormous interest recently because of its useful applications like spin-direction coupling and routing. In this Letter, using the Richards–Wolf vectorial method for standard full Poincaré beams, we present an analytical model for the high-numerical-aperture focusing system to calculate all components of the electric and magnetic field strength vectors as well as spin density and Poynting vector. The role and contribution of the optical degrees of freedom including ellipticity, handedness, and orientation when the transverse spin density is present, are revealed based on this analytical model. Ellipticity affects the localization and magnitude of the transverse spin density for both transverse and longitudinal components. In contrast, handedness only affects the longitudinal component whereas orientation only affects the transverse component. Furthermore, the energy flux in the focal plane are also studied in detail for the standard full Poincaré beams. These findings may be help in spin-controlled directive coupling and optical tweezers.

1. Introduction

The spin density is a quantity describing the spin angular momentum of light field within paraxial approximation, which usually is parallel or antiparallel to the direction of propagation. However, when light fields are analyzed in a three-dimensional confined region, for example, near field radiation [1], strongly focused field [2], surface plasmon polaritons [3–5], two-wave interference [6], and wave-guide modes [7–11], the spin density cannot be treated as scalar because it may have arbitrary orientations. In particular, the local spin density that is perpendicular to the corresponding direction of propagation, is called transverse spin density (TSD) [3] or alternatively a photonic wheel [12].

Most recently, TSD has attracted tremendous interest because of its extraordinary properties [1–19], especially under objective-focusing conditions of high numerical aperture (NA) [20–29]. Many practical applications ranging from storage to microscopy, as well as optical trapping and manipulation of particles, require strong focusing. For example, it has been shown that [21], with a vector beam in an azimuthally varying and locally linear state of polarization (SoP), trapping multiple particles simultaneously and manipulating the particles' spin along the azimuthal direction is possible because of the presence of the TSD. Moreover, the spin torque on the particle may be varied by changing the polarization mode of the input field. When another input field in a SoP described by the square of the azimuthal angle are introduced, the trapped Rayleigh particle may be spun asymmetrically because of the asymmetrical TSD [23]. Not only is spin-to-orbital angular momentum conversion possible, but the converse process, namely, orbital-to-spin conversion, has also been reported. In this optical process, orbital angular momentum can induce a localized spin angular momentum in the strong focusing of spin-free linearly, radially, azimuthally, and higher-order cylindrically polarized beams [22,25–28]. The structured spin angular momentum of the focused field is transferred to the optical torque for the absorptive particle, resulting in the spinning of the trapped particles around its own axis [22,28]. In addition, for the TSD of various kinds of polarized beams in a single-lens high NA focusing system, the performance of structured input fields consisting of radially and azimuthally polarized beams in the 4π focusing system have also been investigated [24]. Most importantly, the spin density of an electromagnetic field near focus is now physically measurable [30,31]. However, when the input field is spin-free, the other optical degrees of freedom (DoFs) including ellipticity and handedness of the polarization are not considered and exploited. Therefore, revealing the roles and contributions of these two polarization DoFs in the modulation of the TSD is warranted. Moreover, as another DoF, orientation should also be explored when TSD is present.

* Corresponding author at: School of Physics and Optoelectronic Engineering, Shandong University of Technology, Zibo 255000, China.
E-mail address: zsman@sdut.edu.cn (Z. Man).

In this Letter, we analyze the effect of input ellipticity, handedness, and orientation on the local spin and energy flux distributions within a tightly focused field of the standard full Poincaré beams. Using the Richards–Wolf vectorial method for the standard full Poincaré beams, we establish an analytical model for a high-numerical-aperture focusing system and evaluate all components of the electric and magnetic field strengths, as well as the spin density and Poynting vector near focus. The role and contribution of the optical DoFs including ellipticity, handedness, and orientation of the TSD when present are studied based on this analytical model. Ellipticity affects the localization and magnitude of the TSD for both transverse and longitudinal components. In contrast, handedness only affects the longitudinal component whereas orientation only affects the transverse component. Furthermore, the energy flux in the focal plane are also studied in detail for the standard full Poincaré beams. These findings may be help in implementing a spin-controlled directed coupling and optical tweezers.

2. Standard full Poincaré beams and corresponding tight-focusing analytical model

To describe all possible SoPs of a polarized plane-wave, the Poincaré sphere (PS) provides a prominent geometric representation, pioneered by Poincaré in 1892, where the SoP is represented by a point on the surface [32]. The three variables, s_1, s_2, and s_3, represent the Stokes parameters of any point in the Cartesian coordinate system, and 2Φ and 2Θ denote, respectively, the longitude and latitude of the point in spherical coordinate system. The north and south poles correspond to right- and left-handed circular polarization, the equator linear polarization, and intermediate points between the poles and equators elliptical polarization. The northern and southern hemispheres separate right- and left-handed ellipticity. For arbitrary meridian circles [Fig. 1(a)], the orientations of the SoPs produce no change although changes in ellipticity from the south to the north poles are seen in Fig. 1(b) where positive and negative values represent left-handed and right-handed SoPs, respectively

For any given polarized optical field, its corresponding SoP in theory may be described by a combination of a pair of orthogonal base vectors. Mathematically, all SoPs on the standard PS [Fig. 1(a)] may be described in the Cartesian coordinate system as a unit vector given by [33–41]

$$\mathbf{V} = \frac{1}{\sqrt{2}} \left[\exp(ja) \left(\cos b \mathbf{e}_x + \sin b \mathbf{e}_y \right) + \exp(-ja) \left(-\sin b \mathbf{e}_x + \cos b \mathbf{e}_y \right) \right], \quad (1)$$

where both a and b are constants, controlling the ellipticity and orientation, respectively. The unit vectors, $\mathbf{e}_x$ and $\mathbf{e}_y$, are directed along the x and y axes, respectively.

Consider an aplanatic high-NA focusing system with focal length f and geometric focus located at the origin of a cylindrical coordinate system in the image space. When the input field with polarization distribution represented by Eq. (1) is incident upon this focusing system, then based on the Richards–Wolf vectorial diffraction theory, the electric field at any point $P(r_P, \phi_P, z_P)$ near focus can be expressed as [42]

$$\mathbf{E}(r_P, \phi_P, z_P) = \begin{bmatrix} E_x(r_P, \phi_P, z_P) \\ E_y(r_P, \phi_P, z_P) \\ E_z(r_P, \phi_P, z_P) \end{bmatrix}$$
$$= -\frac{ikf}{2\pi} \int_0^\alpha \int_0^{2\pi} \sqrt{\cos\theta} l_0(\theta) K(\varphi, \theta) \mathbf{M}_E \sin\theta \, d\varphi \, d\theta. \quad (2)$$

Here k is the wavenumber in the image space and equals $2\pi/\lambda$, λ being the wavelength; the semi-aperture angle is $\alpha = \arcsin(\mathrm{NA}/n)$, NA being the numerical aperture of the objective lens and n the refractive index in the image space. For our focusing system, we chose NA = 0.95 and $n = 1$. The angles φ and θ denote, respectively, the azimuth with respect to the x axis in the objective space and the polar angle with respect

to the z axis; the function $l_0(\theta)$, which represents the input amplitude distribution, has the form [43]

$$l_0(\theta) = \exp\left[-\beta^2 \left(\frac{\sin\theta}{\sin\alpha}\right)^2\right] J_1\left(2\beta\frac{\sin\theta}{\sin\alpha}\right), \quad (3)$$

where β is the ratio of the pupil radius to the beam waist, which we take as unity in our configuration, J_1 the first-order Bessel function of the first kind, and $K(\varphi, \theta)$ is the focusing propagation factor given by

$$K(\varphi, \theta) = \exp(ik\mathbf{s} \cdot \mathbf{r}_P) = \exp\left\{ik\left[-r_P\sin\theta\cos\left(\varphi - \phi_P\right) + z_P\cos\theta\right]\right\}, \quad (4)$$

where $\mathbf{s} = (-\sin\theta\cos\varphi, -\sin\theta\sin\varphi, \cos\theta)$ is the unit vector of the wave vector, and $\mathbf{r}_P = (r_P\cos\phi_P, r_P\sin\phi_P, z_P)$ is the unit polar vector of point P near focus; r_P, ϕ_P, and z_P are the radial, azimuthal, and longitudinal coordinates, respectively, in the cylindrical coordinate system employed in the image space.

In Eq. (2), $\mathbf{M}_E$ is the electric polarization vector in the strongly focused field and stems from the polarization contribution of the incident light field. When the input SoP is denoted by Eq. (1), the corresponding focusing electric polarization vector is

$$\mathbf{M}_E = \begin{bmatrix} \mathrm{M}_E^x \\ \mathrm{M}_E^y \\ \mathrm{M}_E^z \end{bmatrix}, \quad (5)$$

$$\mathrm{M}_E^x = \frac{1}{\sqrt{2}} \left\{ [\cos(b - \varphi)\cos\theta\cos\varphi - \sin(b - \varphi)\sin\varphi] \exp(ia) - [\sin(b - \varphi)\cos\theta\cos\varphi + \cos(b - \varphi)\sin\varphi] \exp(-ia) \right\}, \quad (6a)$$

$$\mathrm{M}_E^y = \frac{1}{\sqrt{2}} \left\{ [\cos(b - \varphi)\cos\theta\sin\varphi + \sin(b - \varphi)\cos\varphi] \exp(ia) - [\sin(b - \varphi)\cos\theta\sin\varphi - \cos(b - \varphi)\cos\varphi] \exp(-ia) \right\}, \quad (6b)$$

$$\mathrm{M}_E^z = \frac{1}{\sqrt{2}} \left\{ \cos(b - \varphi)\sin\theta\exp(ia) - \sin(b - \varphi)\sin\theta\exp(-ia) \right\}. \quad (6c)$$

The integrations over φ can be accomplished using the identity:
$$\int_0^{2\pi} e^{-ikr_P\sin\theta\cos(\varphi - \phi_P)} e^{im\varphi} d\varphi = 2\pi i^m J_m(-kr_P\sin\theta) e^{im\phi_P}, \quad (7)$$

where J_m is the Bessel function of the first kind of order m. The electric fields near focus then have the following form:

$$E_x(r_P, \phi_P, z_P) = -\frac{ikf}{2\sqrt{2}} \int_0^\alpha \sqrt{\cos\theta} l_0(\theta) \sin\theta \cdot$$
$$\left\{ [\cos b(\cos\theta + 1) J_0(-kr_P\sin\theta) + \cos(b - 2\phi_P) \right.$$
$$\times (1 - \cos\theta) J_2(-kr_P\sin\theta)] e^{ia}$$
$$- [\sin b(\cos\theta + 1) J_0(-kr_P\sin\theta) + \sin(b - 2\phi_P)$$
$$\left. \times (1 - \cos\theta) J_2(-kr_P\sin\theta)] e^{-ia} \right\} e^{ikz_P\cos\theta} d\theta, \quad (8a)$$

$$E_y(r_P, \phi_P, z_P) = -\frac{ikf}{2\sqrt{2}} \int_0^\alpha \sqrt{\cos\theta} l_0(\theta) \sin\theta \cdot$$
$$\left\{ [\sin b(\cos\theta + 1) J_0(-kr_P\sin\theta) - \sin(b - 2\phi_P) \right.$$
$$\times (1 - \cos\theta) J_2(-kr_P\sin\theta)] e^{ia}$$
$$[\cos b(\cos\theta + 1) J_0(-kr_P\sin\theta) - \cos(b - 2\phi_P)$$
$$\left. \times (1 - \cos\theta) J_2(-kr_P\sin\theta)] e^{-ia} \right\} e^{ikz_P\cos\theta} d\theta, \quad (8b)$$

$$E_z(r_P, \phi_P, z_P) = \frac{kf}{\sqrt{2}} \int_0^\alpha \sqrt{\cos\theta} l_0(\theta) \sin^2\theta J_1(-kr_P\sin\theta) \cdot$$
$$[\cos(b - \phi_P) e^{ia} - \sin(b - \phi_P) e^{-ia}] e^{ikz_P\cos\theta} d\theta. \quad (8c)$$

Obviously, all three mutually perpendicular polarization components are nonzero, which means that the local polarization ellipse of the focused field is not purely in the transverse plane or longitudinal plane. We shall systematically explore the spin density evolution characteristics, especially the TSD of the standard full PS beams, in the following sections.

3. Spin density

Aided by the analytical model, we now investigate the spin density of the electric field, which is defined as [14,18]

$$s = \frac{\varepsilon}{4\omega} \mathrm{Im}\left(\mathbf{E}^* \times \mathbf{E}\right), \quad (9)$$
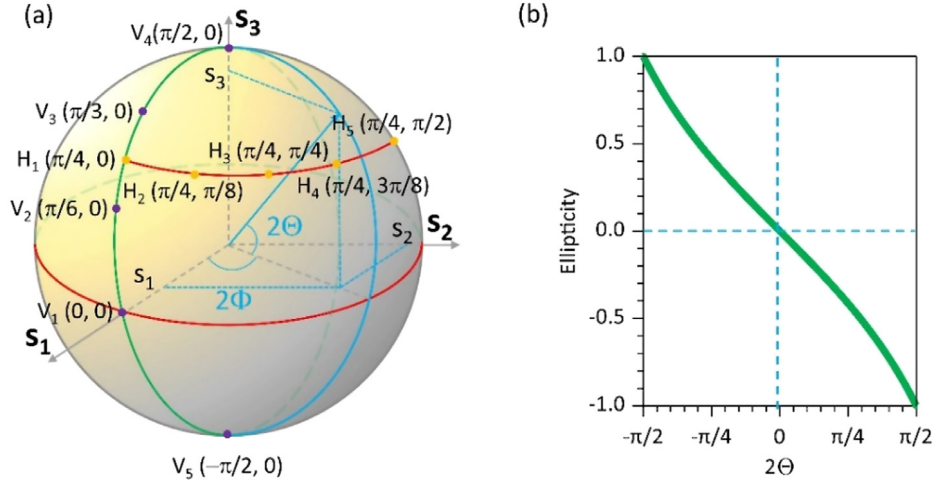
Fig. 1. (a) Standard Poincaré sphere representation for plane waves with arbitrary ellipticity, orientation and handedness. (b) Changes in ellipticity along arbitrary meridian from the south pole to the north pole, where positive and negative values represent the helicity, i.e., left- and right-handed, respectively.

where ε and ω denote, respectively, the permittivity and angular frequency in the image space, the asterisk denotes complex conjugation and Im signifies the operation of extracting the imaginary part from its argument in parentheses. Actually, the spin density is the normal vector of the local polarization ellipse. The direction specifies the handedness (or helicity) of the local ellipse, whereas the absolute value reflects the shape of the polarization ellipse [44,45]. The three orthogonal components in Cartesian coordinate system are given by

$$s = \begin{bmatrix} s_x \\ s_y \\ s_z \end{bmatrix},$$ (10)

$$s_x = \frac{\varepsilon}{4\omega} \text{Im} \left(E_y^* E_z - E_z^* E_y \right),$$ (11a)

$$s_y = \frac{\varepsilon}{4\omega} \text{Im} \left(E_z^* E_x - E_x^* E_z \right),$$ (11b)

$$s_z = \frac{\varepsilon}{4\omega} \text{Im} \left(E_x^* E_y - E_y^* E_x \right).$$ (11c)

Now, we can calculate the spin density of tightly focused standard full PS beams using Eqs. (8a)–(11c); $\lambda = 532$ nm, and $f = 1.6$ mm are used in the following calculations.

First, we explore the effect of two optical DoFs in terms of ellipticity and handedness on the spin density distribution, in particular, the TSD. As examples, we choose five different input beams with SoPs located at the points V_1, V_2, V_3, V_4, and V_5 on the standard PS [Fig. 1]; they correspond to $a = 0$, $\pi/12$, $\pi/6$, $\pi/4$ and $-\pi/4$ and $b = -\pi/4$ in Eq. (1). The calculated spin densities in the focal plane for the x, y, and z components are presented in the upper, middle, and lower rows in Fig. 2. All distributions are normalized by their maximum values of the total spin densities for each input field, to enable a direction comparison of the results. When the SoP changes from V_1 to V_4, the direction of the long axis of the polarization ellipse and handedness remains the same, but the ellipticity changes from 0 to -1 [Fig. 1(b)]. For V_4 and V_5, they have the same ellipticity but opposite handedness. Obviously, both ellipticity and handedness affect the spin density distributions. To be specific, no spin density distribution is obtained for the z component [see Fig. 2(c)] when the input field is spin-free [$a = 0$ and $b = -\pi/4$]; in contrast, they are patterns with four weak lobes [Fig. 2(a)] and two strong lobes [Fig. 2(b)] for the corresponding x and y components, respectively. With increasing ellipticity, the spin density grows for the x and z components but decreases for the y component. Further, the four-lobe pattern evolves into a two-lobe pattern (see first row in Fig. 2). Handedness, however, has no effect on the spin density for both the x [Fig. 2(j) and (m)] and y [Fig. (k) and (n)] components, because they

maintain the opposite handedness [$a = \pm\pi/4$ and $b = \pi/4$] shown in the two far-right columns in Fig. 2. However, a reversed direction for the z component [Fig. 2(l) and (o)], and these directions are actually in line with the input circular polarization.

To better understand the effect of ellipticity and handedness on the TSD, Fig. 3 depicts the normalized cross-sectional spin density distributions on the focal plane of strongly focused input fields with $a = 0$, $\pi/36$, $\pi/18$, $\pi/12$, $\pi/9$, $5\pi/36$, $\pi/6$, $7\pi/36$, $2\pi/9$, $\pi/4$, and $-\pi/4$ when $b = -\pi/4$ for the x component along the y axis direction, the y component along the x axis direction, and the z component along radial direction. All distributions in each image are normalized to their common maximum values. In Fig. 3(a), when $a = 0$, there is no spin density distribution. However, double peaks of opposite values are obvious for other values of a. Moreover, the peak rise rapidly with increasing a. In contrast, the distributions with opposite value for all values of a as illustrated in Fig. 3(a), there is no electric spin density distribution when $a = 0$ for the z component shown in Fig. 3(c), and only one peak arises for other values of a, in contrast to that in Fig. 3(a) and (b). Most importantly, we find the peak exhibits opposite orientation for the opposite handedness.

Next, we study the effect of orientation of the TSD on the high-NA focusing system. As examples, another five input fields with SoPs located at points H_1, H_2, H_3, H_4, and H_5 on the standard PS (Fig. 1) were chosen, corresponding to $b = -\pi/4$, $-\pi/8$, 0, $\pi/8$, and $\pi/4$ when $a = -\pi/8$ in Eq. (1). With SoP changing from H_1 to H_5, the handedness and ellipticity retain unchanged but the angle between the long axis of the polarization ellipse and the x axis changes from 0 to $\pi/4$, implying that the orientation of the SoP changes. The corresponding calculated spin density in the focal plane for the x, y, and z components are shown, respectively, in the upper, middle, and lower rows in Fig. 4. Again, all distributions are normalized by their maximum values of the total spin densities for each input field to enable a direct comparison between the results obtained from the five beams. Obviously, the optical DoF of orientation mainly affects the TSD but has no effect on the longitudinal spin density distributions. Although they are always two-lobed patterns for both the x and y components of the spin density for arbitrary values of b when $a = -\pi/8$, the strength and location are different with different input orientations. Therefore, the DoF of orientation may be used to control the rotation of the spin density for both the x and y components. Here, two rotational angles in terms of ϕ_x and ϕ_y with meaning illustrated in Fig. 4(d) and (e) are introduced to present a detailed study of the rotational properties of the TSD. The x component of spin density first rotates clockwise and then counterclockwise when b increases from $-\pi/4$ to $\pi/4$. The y component, in contrast, first rotates counterclockwise and then clockwise. These trends are evident
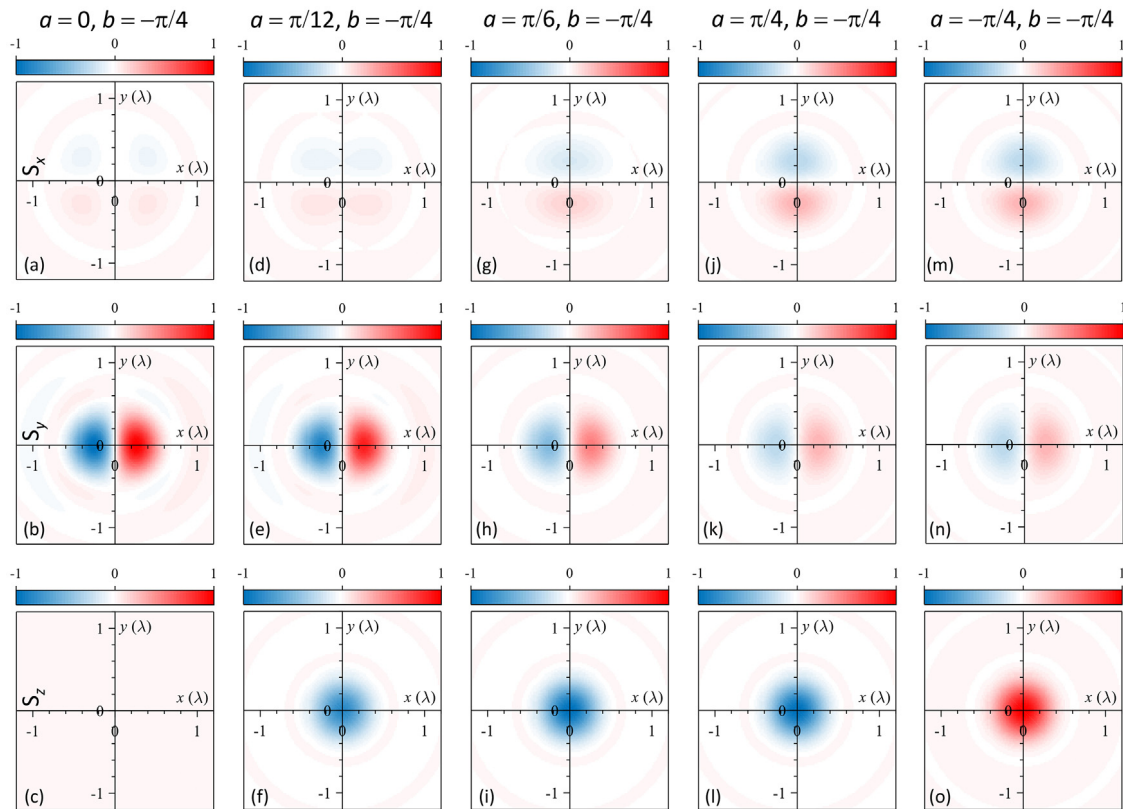
Fig. 2. Theory-derived spin density distributions of the electric field in the focal plane of five tightly focused input fields with $a = 0$, $\pi/12$, $\pi/6$, $\pi/4$ and $-\pi/4$; $b = -\pi/4$. The input field is linearly polarized when $a = 0$ and circularly polarized when $a = \pi/4$ and $-\pi/4$. For $a = \pi/12$ and $\pi/6$, it is elliptically polarized. The upper, middle, and lower rows depict the x, y, and z components of the spin density, respectively. All distributions are normalized by their maximum values of the total spin densities for each input field to enable a direction comparison between the five beams.
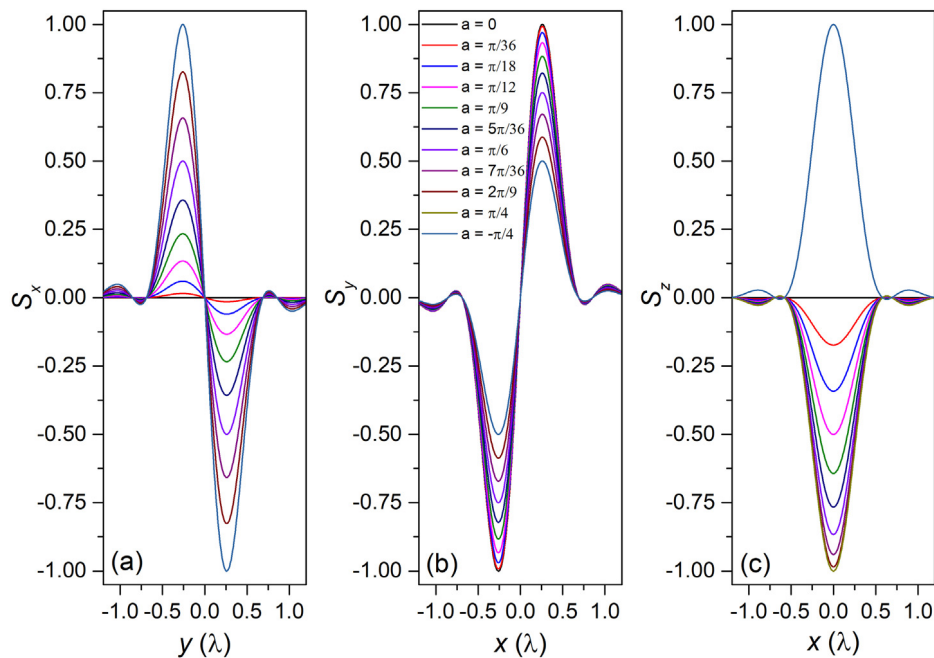

Fig. 3. Normalized cross-sectional electric spin density distributions on the focal plane of strongly focused input fields with $a = 0$, $\pi/36$, $\pi/18$, $\pi/12$, $\pi/9$, $5\pi/36$, $\pi/6$, $7\pi/36$, $2\pi/9$, $\pi/4$, and $-\pi/4$ when $b = -\pi/4$ for (a) x component along y axis direction, (b) y component along x axis direction, and (c) z component along radial direction. The distributions in all plots are normalized by their common maximum values.
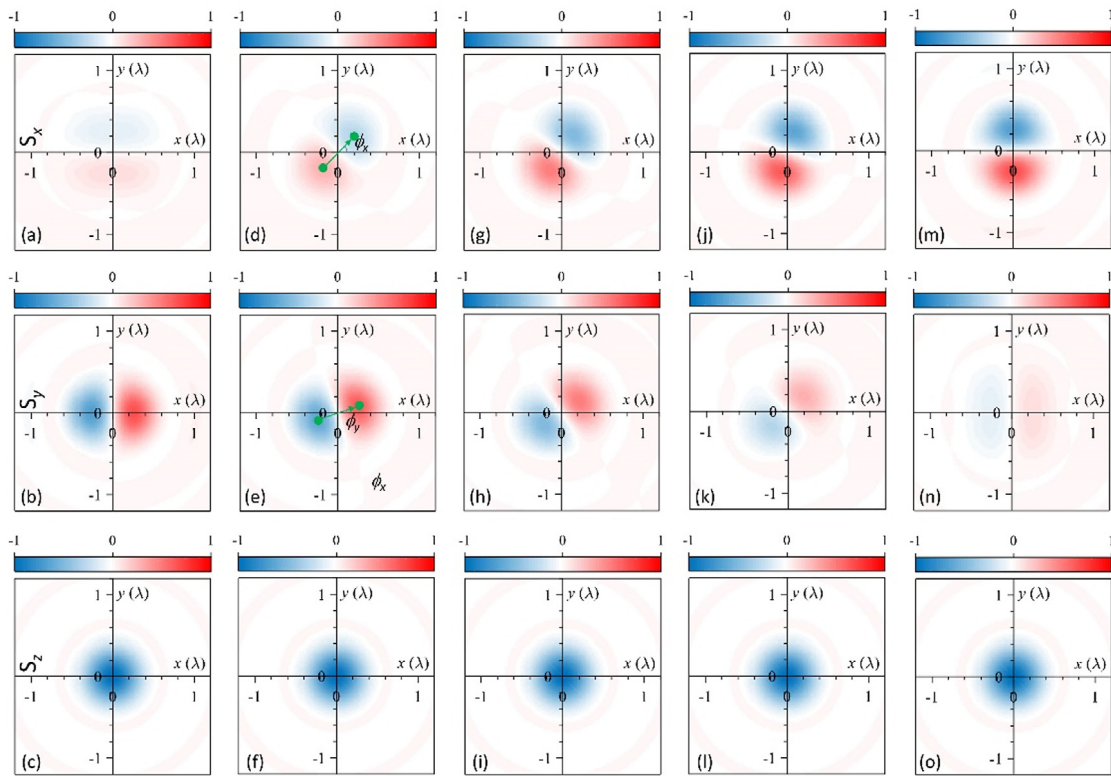
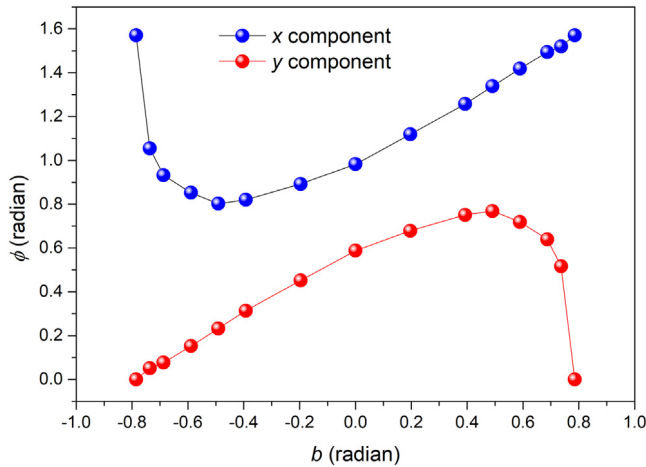**Fig. 4.** Same as for Fig. 2 but with $b = -\pi/4$, $-\pi/8$, 0, $\pi/8$, and $\pi/4$ when $a = -\pi/8$.

Fig. 5. Rotational angles ϕ_x and ϕ_y with meaning illustrated, respectively, in Fig. 4(d) and (e) versus parameter b when $a = -\pi/8$.

in Fig. 5. The inflection points of the directional rotation for the x and y components are calculated to be about $(b, \phi_{x,y}) = (-0.4909, 0.8023)$ and $(0.4909, 0.7685)$, respectively.

4. Energy flux

The TSD can be used to control the trapped particles to spin around its own axis. In contrary, the energy flux in the focal plane of the optical field is also useful, because it can be used to control the transport of absorptive particles along certain paths. Similarly, the corresponding magnetic field at any point $P(r_P, \phi_P, z_P)$ near focus can be expressed

as [42]

$$\mathbf{H}(r_P, \phi_P, z_P) = \begin{bmatrix} H_x(r_P, \phi_P, z_P) \\ H_y(r_P, \phi_P, z_P) \\ H_z(r_P, \phi_P, z_P) \end{bmatrix}$$
$$= -\frac{ikf}{2\pi} \int_0^\alpha \int_0^{2\pi} \sqrt{\cos\theta} l_0(\theta) K(\varphi, \theta) \mathbf{M}_H \sin\theta \, d\varphi \, d\theta, \quad (12)$$

where $\mathbf{M}_H$ is the magnetic polarization vector in the tightly focused field given by

$$\mathbf{M}_H = \begin{bmatrix} \mathrm{M}_H^x \\ \mathrm{M}_H^y \\ \mathrm{M}_H^z \end{bmatrix}, \quad (13)$$

$$\mathrm{M}_H^x = \sqrt{\frac{\varepsilon}{2\mu}} \left\{ [-\sin(b-\varphi)\cos\theta\cos\varphi - \cos(b-\varphi)\sin\varphi]\exp(ia) - [\cos(b-\varphi)\cos\theta\cos\varphi - \sin(b-\varphi)\sin\varphi]\exp(-ia) \right\}, \quad (14a)$$

$$\mathrm{M}_H^y = \sqrt{\frac{\varepsilon}{2\mu}} \left\{ [-\sin(b-\varphi)\cos\theta\sin\varphi + \cos(b-\varphi)\cos\varphi]\exp(ia) - [\cos(b-\varphi)\cos\theta\sin\varphi + \sin(b-\varphi)\cos\varphi]\exp(-ia) \right\}, \quad (14b)$$

$$\mathrm{M}_H^z = \sqrt{\frac{\varepsilon}{2\mu}} \left\{ -\sin(b-\varphi)\sin\theta\exp(ia) - \cos(b-\varphi)\sin\theta\exp(-ia) \right\}, \quad (14c)$$

where μ represents the permeability in the image space. The integrations over φ can be accomplished as before, yielding

$$H_x(r_P, \phi_P, z_P) = -\frac{ikf\sqrt{\varepsilon/\mu}}{2\sqrt{2}} \int_0^\alpha \sqrt{\cos\theta} l_0(\theta)\sin\theta \cdot$$
$$\left\{ [-\sin b(\cos\theta + 1) J_0(-kr_P\sin\theta) - \sin(b - 2\phi_P) \right.$$
$$\times (1 - \cos\theta) J_2(-kr_P\sin\theta)] e^{ia}$$
$$- [\cos b(\cos\theta + 1) J_0(-kr_P\sin\theta) + \cos(b - 2\phi_P)$$
$$\left. \times (1 - \cos\theta) J_2(-kr_P\sin\theta)] e^{-ia} \right\} e^{ikz_P\cos\theta} d\theta, \quad (15a)$$
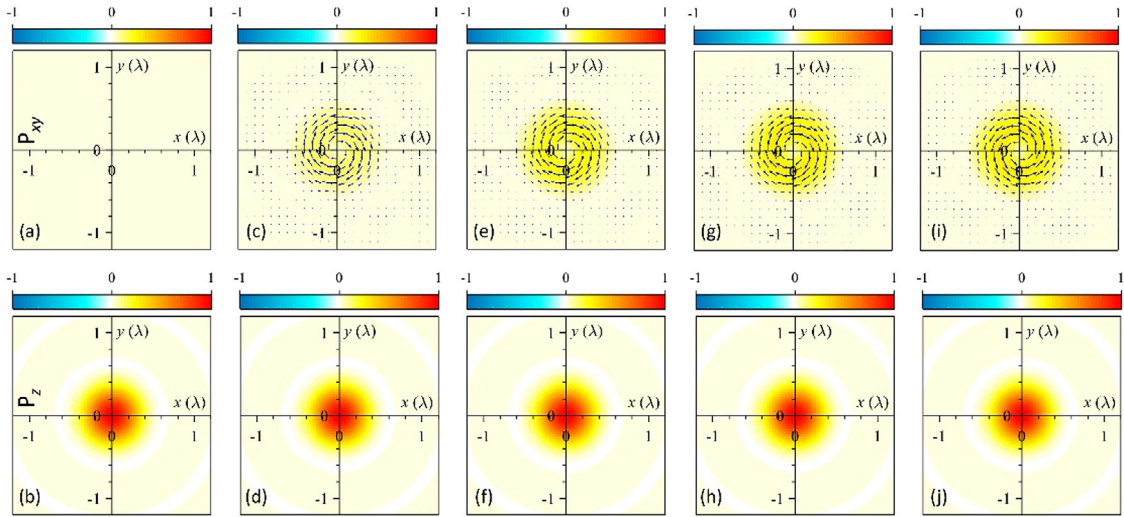
Fig. 6. Theory-derived Poynting vector in the focal plane of tightly focused input fields with $a = 0$, $\pi/12$, $\pi/6$, $\pi/4$ and $-\pi/4$ when $b = -\pi/4$. The upper and lower rows depict the transverse and longitudinal components of the energy flux, respectively. All distributions of the energy flux are normalized to their maximum values of the total energy flux for each input field to enable a direct comparison between the five beams.
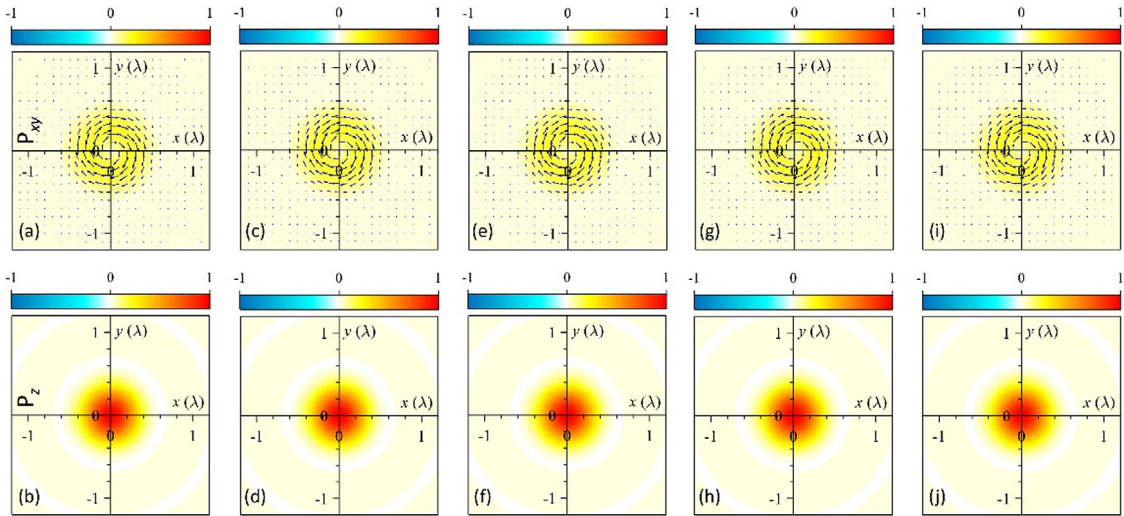

Fig. 7. Same as for Fig. 6 but with $b = -\pi/4$, $-\pi/8$, 0, $\pi/8$, and $\pi/4$ when $a = -\pi/8$.

$$H_y(r_P, \phi_P, z_P) = -\frac{ikf\sqrt{\epsilon/\mu}}{2\sqrt{2}} \int_0^\alpha \sqrt{\cos\theta} l_0(\theta) \sin\theta \cdot$$
$$\left\{ \left[\cos b (\cos\theta + 1) J_0(-kr_P \sin\theta) - \cos(b - 2\phi_P) \right. \right.$$
$$\times (1 - \cos\theta) J_2(-kr_P \sin\theta) \right] e^{ia}$$
$$- \left[\sin b (\cos\theta + 1) J_0(-kr_P \sin\theta) - \sin(b - 2\phi_P) \right.$$
$$\left. \left. \times (1 - \cos\theta) J_2(-kr_P \sin\theta) \right] e^{-ia} \right\} e^{ikz_P \cos\theta} d\theta, \tag{15b}$$

$$H_z(r_P, \phi_P, z_P) = \frac{kf\sqrt{\epsilon/\mu}}{\sqrt{2}} \int_0^\alpha \sqrt{\cos\theta} l_0(\theta) \sin 2\theta J_1(-kr_P \sin\theta) \cdot$$
$$\left[-\sin(b - \phi_P) e^{ia} - \cos(b - \phi_P) e^{-ia} \right] e^{ikz_P \cos\theta} d\theta. \tag{15c}$$

In term of the three-dimensional electric and magnetic fields, the energy flux is given by the time-averaged Poynting vector [46,47]

$$\mathbf{P} \propto \text{Re}\left(\mathbf{E} \times \mathbf{H}^*\right), \tag{16}$$

where Re signifies the operation of extracting the real part of the argument. We calculate the energy flux of the tightly focused standard full Poincaré beams using Eqs. (8a)–(8c) and Eqs. (15a)–(16).

We next discuss the effect of the optical DoFs including ellipticity and handedness on the energy flux. By calculation, we find that both ellipticity and handedness mainly affect the transverse energy flow, and the longitudinal energy flow remains almost unchanged regardless of ellipticity and handedness. The Poynting vectors of the five tightly focused electric fields mentioned in Fig. 2 are drawn in Fig. 6. We see that the transverse energy flow is zero for a spin-free input field ($a = 0$), whereas for other values of a this flow exists and always exhibits a doughnut-shaped pattern [Fig. 6(c), (e), (g), and (i)], arising from the spin-to-orbital angular momentum conversion [48,49]. Furthermore, the magnitude of the transverse component of the Poynting vector, compared with the longitudinal component [Fig. 6(b), (d), (f), (h), and (i)], gradually increases as |a| increases. As a result, transporting a particle in the transverse plane becomes easier. Moreover, we find that the handedness of the input field only affects the direction of the transverse energy flow and has no effect on the magnetic field [Fig. 6(g) and (i)]. In contrast to the optical DoFs, i.e., ellipticity and handedness, orientation has no effect on both the transverse and longitudinal energy flows (see Fig. 7 depicting the energy flux in the focal plane of five input fields mentioned in Fig. 4). Apparently, the transverse energy, which has a ring-shaped pattern, always exhibits the same magnitude and direction with a change of input orientation (upper row in Fig. 7). Similarly, the longitudinal energy flow has a hot spot located on-axis (lower row in Fig. 7).

5. Conclusions

To summarize, we revealed the effect of input ellipticity, handedness, and orientation on the local spin density and energy flux distributions within the tightly focused field of standard full Poincaré beams. Using the Richards–Wolf vectorial method for standard full Poincaré beams, we presented an analytical model for the high-numerical-aperture focusing system to evaluate all vector components of the electric and magnetic field strength, as well as the spin density and Poynting vector near focus. By numerically calculating the spin density and energy flux on the focal plane based on our analytical model, we demonstrated that ellipticity affects the distributions of the spin density for both transverse and longitudinal components. In contrast, handedness only affects the longitudinal component whereas orientation only affects the transverse component. Furthermore, the magnitude and shape of the transverse energy flux were determined using the ellipticity whereas its direction is collinear with the input handedness. All three DoFs including ellipticity, handedness, and orientation have nearly no effect on the longitudinal energy flow. These findings may help in applications involving spin-controlled directed coupling and optical tweezers.

References

[1] S. Saha, A.K. Singh, S.K. Ray, A. Banerjee, S.D. Gupta, N. Ghosh, Transverse spin and transverse momentum in scattering of plane waves, Opt. Lett. 41 (2016) 4499–4502.

[2] J. Chen, C. Wan, L.J. Kong, Q. Zhan, Tightly focused optical field with controllable photonic spin orientation, Opt. Express 25 (2017) 19517–19527.

[3] K.Y. Bliokh, F. Nori, Transverse spin of a surface polariton, Phys. Rev. A 85 (2012) 061801.

[4] K.Y. Kim, I.M. Lee, J. Kim, J. Jung, B. Lee, Time reversal and the spin angular momentum of transverse electric and transverse-magnetic surface modes, Phys. Rev. A 86 (2012) 063805.

[5] A. Canaguier-Dur, C. Genet, Transverse spinning of a sphere in a plasmonic field, Phys. Rev. A 89 (2014) 033841.

[6] A.Y. Bekshaev, K.Y. Bliokh, F. Nori, Transverse spin and momentum in two-wave interference, Phys. Rev. X 5 (2015) 011039.

[7] J. Petersen, J. Volz, A. Rauschenbeutel, Chiral nanophotonic waveguide interface based on spin-orbit interaction of light, Science 346 (2014) 67–71.

[8] I. Söllner, S. Mahmoodian, S.L. Hansen, L. Midolo, A. Javadi, G. Kiršanskė, T. Pregnolato, H. El-Ella, E.H. Lee, J.D. Song, S. Stobbe, P. Lodahl, Deterministic photon-emitter coupling in chiral photonic circuits, Nat. Nanotechnol. 10 (2015) 775–778.

[9] A.B. Young, A.C.T. Thijssen, D.M. Beggs, P. Androvitsaneas, L. Kuipers, J.G. Rarity, S. Hughes, R. Oulton, Polarization engineering in photonic crystal waveguides for spin-photon entanglers, Phys. Rev. Lett. 115 (2015) 153901.

[10] P. Lodahl, S. Mahmoodian, S. Stobbe, A. Rauschenbeutel, P. Schneeweiss, J. Volz, H. Pichler, P. Zoller, Chiral quantum optics, Nature 541 (2017) 473.

[11] M.F. Picardi, K.Y. Bliokh, F.J. Rodríguez-Fortuño, F. Alpeggiani, F. Nori, Angular momenta, helicity, and other properties of dielectric-fiber and metallic-wire modes, Optica 5 (2018) 1016–1026.

[12] A. Aiello, P. Banzer, M. Neugebauer, G. Leuchs, From transverse angular momentum to photonic wheels, Nat. Photonics 9 (2015) 789–795.

[13] K.Y. Bliokh, A.Y. Bekshaev, F. Nori, Dual electromagnetism: helicity, spin, momentum and angular momentum, New J. Phys. 15 (2013) 033026.

[14] K.Y. Bliokh, A.Y. Bekshaev, F. Nori, Extraordinary momentum and spin in evanescent waves, Nature Commun. 5 (2014) 3300.

[15] K.Y. Bliokh, J. Dressel, F. Nori, Conservation of the spin and orbital angular momenta in electromagnetism, New J. Phys. 16 (2014) 093037.

[16] K.Y. Bliokh, F. Nori, Transverse and longitudinal angular momenta of light, Phys. Rep. 592 (2015) 1–38.

[17] K.Y. Bliokh, F.J. Rodríguez-Fortuño, F. Nori, A.V. Zayats, Spin–orbit interactions of light, Nat. Photonics 9 (2015) 796–808.

[18] T. Bauer, M. Neugebauer, G. Leuchs, P. Banzer, Optical polarization Möbius strips and points of purely transverse spin density, Phys. Rev. Lett. 117 (2016) 013601.

[19] J. Hu, T. Xia, X. Cai, S. Tian, H. Guo, S. Zhuang, Right- and left-handed rules on the transverse spin angular momentum of a surface wave of photonic crystal, Opt. Lett. 42 (2017) 2611–2614.

[20] W. Zhu, W. She, Transverse angular momentum and transverse barycenter shift of a focused light field due to nonuniform input angular momentum, Opt. Lett. 39 (2014) 1337–1340.

[21] M. Li, S. Yan, Y. Liang, P. Zhang, B. Yao, Transverse spinning of particles in highly focused vector vortex beams, Phys. Rev. A 95 (2017) 053802.

[22] P. Shi, L. Du, X. Yuan, Structured spin angular momentum in highly focused cylindrical vector vortex beams for optical manipulation, Opt. Express 26 (2018) 23449–23459.

[23] Y. Zhang, Y. Xue, Z. Zhu, G. Rui, Y. Cui, B. Gu, Theoretical investigating on asymmetrical spinning and orbiting motions of particles in a tightly focused power-exponent azimuthal-variant vector field, Opt. Express 26 (2018) 4318–4329.

[24] W. Yan, Z. Nie, X. Liu, X. Zhang, Y. Wang, Y. Song, Arbitrarily spin-orientated and super-resolved focal spot, Opt. Lett. 43 (2018) 3826–3829.

[25] P. Yu, Q. Zhao, X. Hu, Y. Li, L. Gong, Orbit-induced localized spin angular momentum in the tight focusing of linearly polarized vortex beams, Opt. Lett. 43 (2018) 5677–5680.

[26] X. Pang, W. Miao, Spinning spin density vectors along the propagation direction, Opt. Lett. 43 (2018) 4831–4834.

[27] L. Han, S. Liu, P. Li, Y. Zhang, H. Cheng, J. Zhao, Catalystlike effect of orbital angular momentum on the conversion of transverse to three-dimensional spin states within tightly focused radially polarized beams, Phys. Rev. A 97 (2018) 053802.

[28] M. Li, Y. Cai, S. Yan, Y. Liang, P. Zhang, B. Yao, Orbit-induced localized spin angular momentum in strong focusing of optical vectorial vortex beams, Phys. Rev. A 97 (2018) 053842.

[29] G. Rui, Y. Li, S. Zhou, Y. Wang, B. Gu, Y. Cui, Q. Zhan, Optically induced rotation of Rayleigh particles by arbitrary photonic spin, Photon. Res. 7 (2019) 69–79.

[30] M. Neugebauer, T. Bauer, A. Aiello, P. Banzer, Measuring the transverse spin density of light, Phys. Rev. Lett. 114 (2015) 063901.

[31] M. Neugebauer, J.S. Eismann, T. Bauer, P. Banzer, Magnetic and electric transverse spin density of spatially confined light, Phys. Rev. X 8 (2018) 022042.

[32] H. Poincaré, Theorie Mathematique de la Lumiere, Gauthiers-Villars, Paris, 1892.

[33] Q. Zhan, Cylindrical vector beams: from mathematical concept to applications, Adv. Opt. Photon. 1 (2009) 1–57.

[34] G. Milione, H.I. Sztul, D.A. Nolan, R.R. Alfano, Higher-order Poincaré sphere, Stokes parameters, and the angular momentum of light, Phys. Rev. Lett. 107 (2011) 053601.

[35] C. Maurer, A. Jesacher, S. Fürhapter, S. Bernet, M. Ritsch-Marte, Tailoring of arbitrary optical vector beams, New J. Phys. 9 (2007) 78.

[36] X. Wang, J. Ding, W. Ni, C. Guo, H. Wang, Generation of arbitrary vector beams with a spatial light modulator and a common path interferometric arrangement, Opt. Lett. 32 (2007) 3549–3551.

[37] D. Naidoo, F.S. Roux, A. Dudley, I. Litvin, B. Piccirillo, L. Marrucci, A. Forbes, Controlled generation of higher-order Poincaré sphere beams from a laser, Nature Photon. 10 (2016) 327.

[38] Z. Liu, Y. Liu, Y. Ke, Y. Liu, W. Shu, H. Luo, S. Wen, Generation of arbitrary vector vortex beams on hybrid-order Poincaré sphere, Photon. Res. 5 (2017) 15–21.

[39] L. Li, C. Chang, C. Yuan, S. Feng, S. Nie, Z. Ren, H. Wang, J. Ding, High efficiency generation of tunable ellipse perfect vector beams, Photon. Res. 6 (2018) 1116–1123.

[40] D. Xu, B. Gu, G. Rui, Q. Zhan, Y. Cui, Generation of arbitrary vector fields based on a pair of orthogonal elliptically polarized base vectors, Opt. Express 24 (2016) 4177–4186.

[41] X.L. Wang, Y.N. Li, J. Chen, C.S. Guo, J.P. Ding, H.T. Wang, A new type of vector field with hybrid states of polarization, Opt. Express 18 (2010) 10786–10795.

[42] B. Richards, E. Wolf, Electromagnetic diffraction in optical systems II, structure of the image field in an aplanatic system, Proc. Roy. Soc. A 253 (1959) 358–379.

[43] K.S. Youngworth, T.G. Brown, Focusing of high numerical aperture cylindrical vector beams, Opt. Express 7 (2000) 77–87.

[44] M.V. Berry, M.R. Dennis, Polarization singularities in isotropic random vector waves, Proc. R. Soc. A 457 (2001) 141–155.

[45] M.V. Berry, Index formulae for singular lines of polarization, J. Opt. A 6 (2004) 675–678.

[46] V.V. Kotlyar, A.A. Kovalev, A.G. Nalimov, Energy density and energy flux in the focus of an optical vortex: reverse flux of light energy, Opt. Lett. 43 (2018) 2921–2924.

[47] Z. Man, Z. Bai, S. Zhang, X. Li, J. Li, X. Ge, Y. Zhang, S. Fu, Redistributing the energy flow of a tightly focused radially polarized optical field by designing phase masks, Opt. Express 26 (2018) 23935–23944.

[48] Y. Zhao, J. Scott Edgar, G.D.M. Jeffries, D. McGloin, D.T. Chiu, Spin-to-orbital angular momentum conversion in a strongly focused optical beam, Phy. Rev. Lett. 99 (2007) 073901.

[49] K.Y. Bliokh, F.J. Rodríguez-Fortuño, F. Nori, A.V. Zayats, Spin–orbit interaction of light, Nature Photon. 9 (2015) 796–808.